Calorimeter Electronics Upgrade for Run 2

Technical Design Report
Version 1.7
May 18, 1998

Columbia University, New York, NY 10027.
Fermi National Accelerator Laboratory , Batavia, Illinois 60510.
Laboratoire de L'Accelerateur Lineaire, France
LPNHE, Universites Paris VI and VII, France
State University of New York, Stony Brook, NY 11794.

Contents

List of Figures

1 Introduction

The DØ experiment at the Fermilab Tevatron $p\bar{p}$ collider is a general purpose collider detector experiment, built to study proton-antiproton collisions at the center-of-mass energy of 1.8 TeV. One of the salient components of this detector is a hermetic, highly stable, radiation-hard liquid argon calorimeter. Depleted Uranium is used as the absorber material in the electromagnetic and the inner hadronic sections of the calorimeter, because of its high density and compensating e/π response. The calorimeter consists of three units, the Central Calorimeter (CC) and the two End-cap Calorimeters (EC), each of which is contained in its own cryostat.

Test-beam data have shown that the energy resolution of the electromagnetic calorimeter due to stochastic fluctuations of the electromagnetic showers can be characterized as $S/\sqrt{E}$, where S is measured to be 14%, 14.6% and 17.8% at pseudorapidity η=0.05, η=0.45 and η=1.05 respectively in the CC [1]. In the EC the electrons are incident almost normally and the stochastic resolution can be characterized as $15.7\%/\sqrt{E}$, where E is the energy of the electron [2]. For high transverse momentum particles such as electrons produced by the decay of W and Z particles, the stochastic component of the resolution is about 2%. The unit gain of the liquid argon calorimeter helps to keep the response highly stable over time. In order to fully exploit these qualities of the calorimeter and achieve good energy scale accuracy and resolution, it is essential that the calorimeter readout electronics be highly linear, stable and produce very little electronic noise.

During run 1, the calorimeter electronics performed very well and helped to ensure that the contribution of the channel-to-channel calibration uncertainty to the electromagnetic energy resolution (constant term) was no more than 1%. The excellent accuracy and resolution of the calorimeter allows DØ to make precision measurements with electrons, photons and jets in the absence of a magnetic tracker. Furthermore, because of the small coherent noise in the system, the resolution of the total transverse energy in the event is sufficiently good that the transverse momentum of an undetected neutrino in the event is "measured" by imposing transverse momentum balance. Hence the neutrino is another particle measured in DØ using the calorimeter. DØ has been able to perform measurements of many interesting physical quantities using the calorimeter, including precise measurements of the W boson and top quark masses.

DØ recorded approximately 100 pb^{-1} of integrated luminosity during run 1. The average instantaneous luminosity recorded by DØ during Run 1b was 7.4×10^{30}/cm^2/s. The peak instantaneous luminosity was greater than 25×10^{30}/cm^2/s. Starting in 1999, the Fermilab Main Injector will be able to provide much higher instantaneous luminosities, the nominal goal being to deliver the instantaneous luminosity of 2×10^{32}/cm^2/s. This will provide the opportunity to collect over 20 times the volume of data that were collected during run 1, with exciting implications for precision measurements and searches for new phenomena.

The goal of the calorimeter electronics upgrade is to modify the calorimeter readout system so that it can perform comparably in the new regime. The higher luminosity in Run II is achieved by reducing the bunch crossing time to 132 ns, from the Run 1 bunch crossing time of 3.5 μs. There are two requirements that need to be satisfied: (i) reduction in the pulse shaping and readout time, and (ii) analog buffering needed to store data until the level-1 trigger decision is available. These tasks needs to be performed while maintaining the properties of low electronic noise, high linearity and good accuracy, i.e. small variations in channel-to-channel response.

The purpose of this report is to document the changes being performed to the electronics to achieve these goals. We first describe the signal path from the calorimeter cell to the analog-to-digital converter (ADC) for one channel, in the current version (Run 1) of the electronics. We then describe the individual components of this data chain, with emphasis on the upgrade versions. Finally, we discuss the physics implications of the upgraded system and its costs. Technical details of various sub-systems can be found in the appendices.

2 Signal Path in the Run 1 Electronics Version

Each calorimeter cell consists of a 2.3 mm liquid argon gap between an absorber plate and a G10 board. The G10 board has a high-resistivity coating, to which a potential is applied with respect to the absorber plate in order to create the drift electric field. The particles traversing the gap produce an ionized trail of electrons and ions. In the electric field the electrons drift towards the G10 coating, producing a current. The current induces an image charge on a copper pad etched on the G10 board under the resistive coat. Successive copper pads are ganged together to form a readout cell.

The signal from each readout cell is brought to a feed-through port on a 30 Ω coaxial cable. The feed-through ports are sealed interfaces between the inside and the outside of the liquid argon cryostats. The feed-through boards reorganize signals from the module-builder's scheme (all η at fixed depth) to the physics scheme in which signals from all depths in an $\eta\phi$ space of 0.2×0.2 are delivered on two 24-channel cables. This eases triggering since all the channels needed to make a trigger tower go to a single 48-channel preamplifier PC board. The signals are carried from the feed-through ports to the preamplifier inputs on 115 Ω twist & flat cables. The preamplifiers are small hybrid ceramic printed circuits, which are themselves mounted on a printed circuit motherboard, 48 to a motherboard. The charge-sensitive preamplifiers integrate the image charge produced by the calorimeter cells to produce proportional voltages. The voltage pulses are carried by 115 Ω twist & flat cables to the shaper and baseline subtracter (BLS).

In these circuits the preamplifier outputs are shaped, sampled before and after the bunch crossing, and the difference is stored on a sample & hold circuit. This baseline subtraction process removes slowly varying offsets in the quiescent input voltage. The sample & hold outputs are then read out and digitized by the ADCs when a trigger is received. A schematic of this data flow path is shown in figure 1.

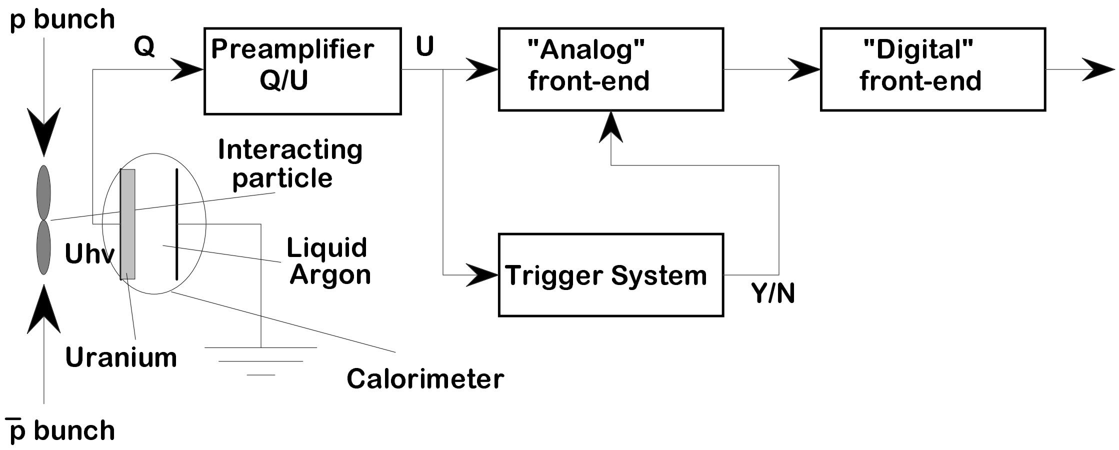

Figure 1: Simplified diagram of the calorimeter data flow path.

3 Modifications for Run 2

We attempted to maintain as much of the infrastructure (i.e. crates and cables) as possible, both to save money and to minimize the effort required to install and debug 55,000 channels. The components that need to be replaced for the upgrade are the cables between the feed-through ports and the preamplifiers, the preamplifiers and their motherboards, the shapers, baseline subtractors (BLS) and sample & holds, the power supplies for both these systems, and a new charge injection pulser system for calibration and monitoring stability. In addition, the timing, trigger and readout control need to be modified to handle the faster timing, higher trigger rates and analog buffering expected in Run 2. The BLS analog driver cards and the ADCs will not be changed. The modifications and their motivation are discussed in the following. The calorimeter part of the data flow and control in Run 2 is shown in figure 2.

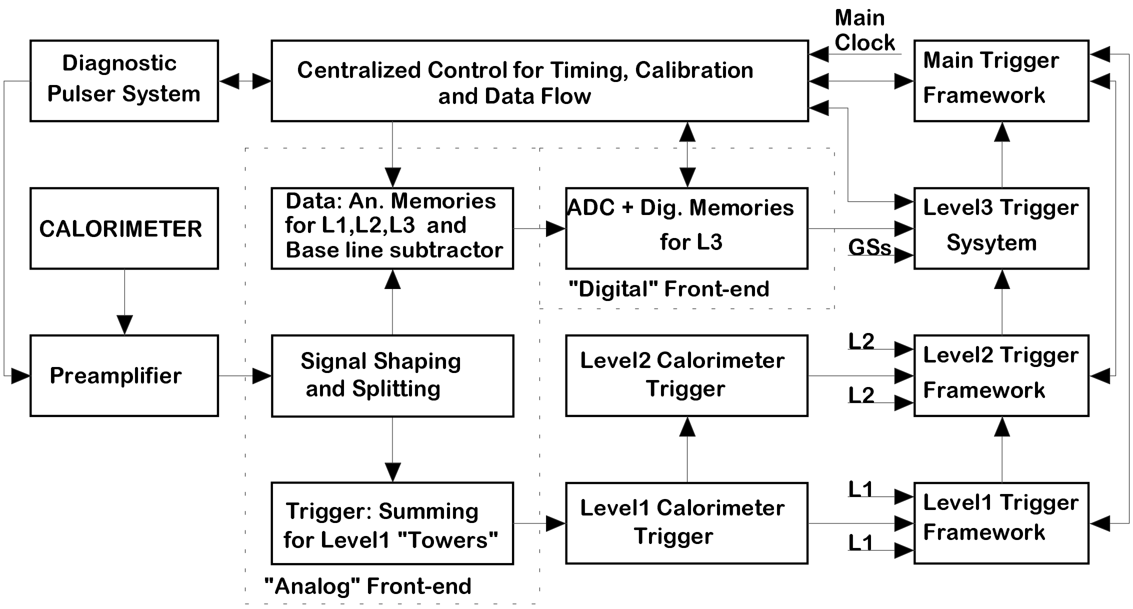

Figure 2: The calorimeter part of the data flow and control in Run 2.

4 The Preamplifier System (WBS 1.2.1.1)

4.1 Preamplifier Input Cables (WBS 1.2.1.6)

The impedance of the cables reading out the calorimeter cells has an impact on the rate at which the charge is extracted from the cells. The planar geometry of the cells causes each readout channel to look like a capacitor at the detector end of the readout cable. This capacitance varies between a few hundred picofarads for the first three electromagnetic layers to a few nanofarads for the hadronic layers. This capacitance and the cable impedance forms an integrating RC circuit that delays the transfer of the image charge produced in the cell into the preamplifier. A cable with lower impedance reduces the RC delay time constant, hence the 30 Ω cable is preferred over the 115 Ω cable.

In Run 1, with 3.5 μs between bunch crossings, high speed timing was not an issue. Hence a staged approach was adopted with respect to the readout cables. The 30 Ω cables were used inside the calorimeter cryostats since the cryostats were not to be opened again. Between the feed-through ports and the preamplifiers, 115 Ω twist & flat cables were used, since these are significantly cheaper.

For the upgrade, the external cables were replaced with multiconductor co-axial 30 Ω cables over the summer of 1996. This was necessary for impedance matching so that the calorimeter pulses do not suffer reflections at the feed-through port interface and to mitigate the RC time constant problem.

The second important point about the readout cables is that the difference in cable lengths for different channels needs to be small compared to the pulse shaping time, to prevent systematic channel-to-channel variations in response. The replacement of the external cables was used as an opportunity to adjust the lengths of the new cables to minimize the total propagation delay differences between calorimeter cells and preamplifiers [1]. The distribution of cable lengths before and after replacement of cables is shown in figures 3 and 4 respectively. The spread in the length of cables is significantly reduced in the CC after replacement of cables [3]. As shown in appendix 13.1, the spread in lengths for the EC electromagnetic channels within each section is also reduced significantly after cable replacement. However the spread for the EC hadronic channels could not be reduced due to the construction of the EC hadronic calorimeter.

In addition to the manufacturer's testing, we tested each cable for good electrical contact. The continuity of the new cables after installation has been checked *in situ* by studying the pedestal widths and the channel response to injected charge. A contribution

[1] In Run 1, there wasn't sufficient space to accomodate the required lengths of the twist & flat cables to equalize the lengths, the twist & flat cables being bulkier than the 30 Ω co-axial cables.

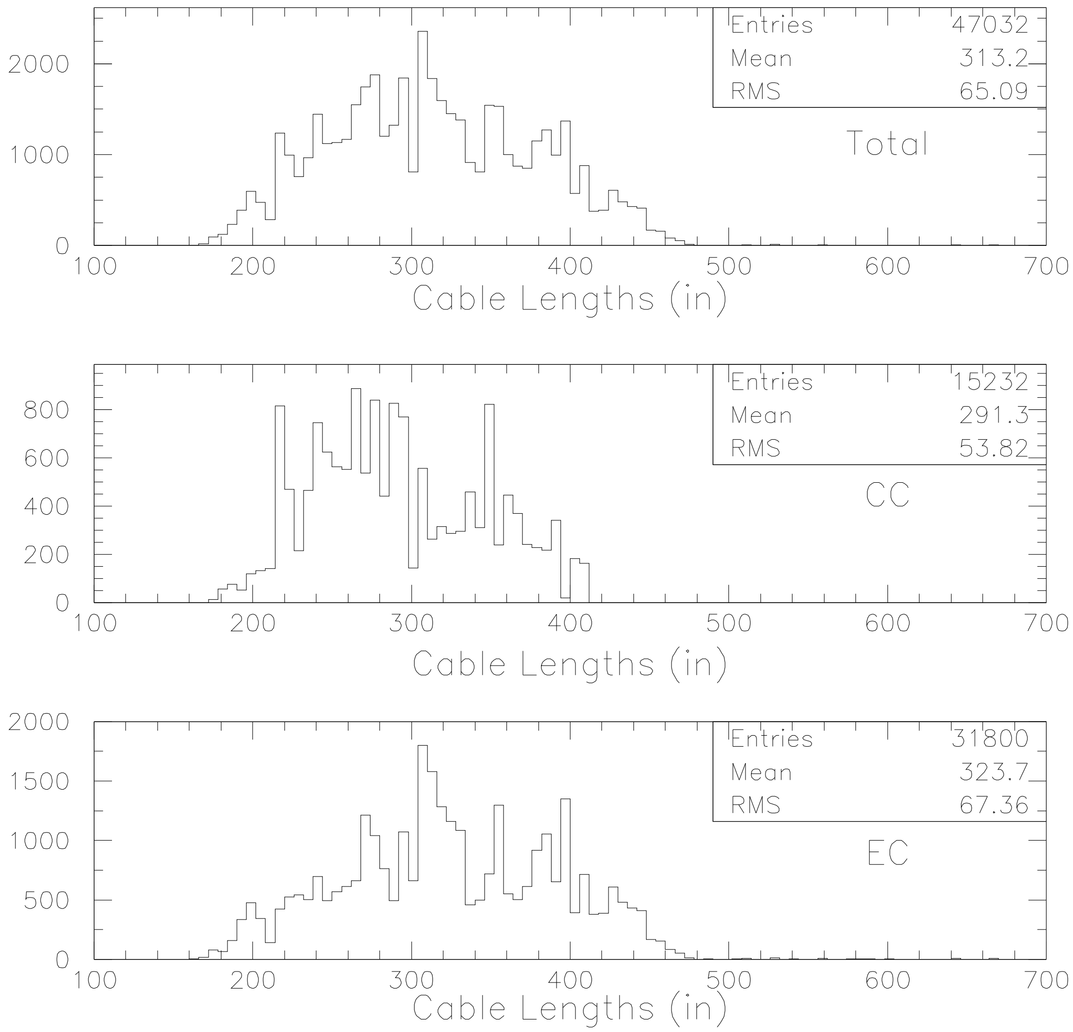

Figure 3: Distribution of preamplifier input cable length for all channels (top), CC channels only (middle) and EC channels only (bottom). This is for the Run 1 cables.

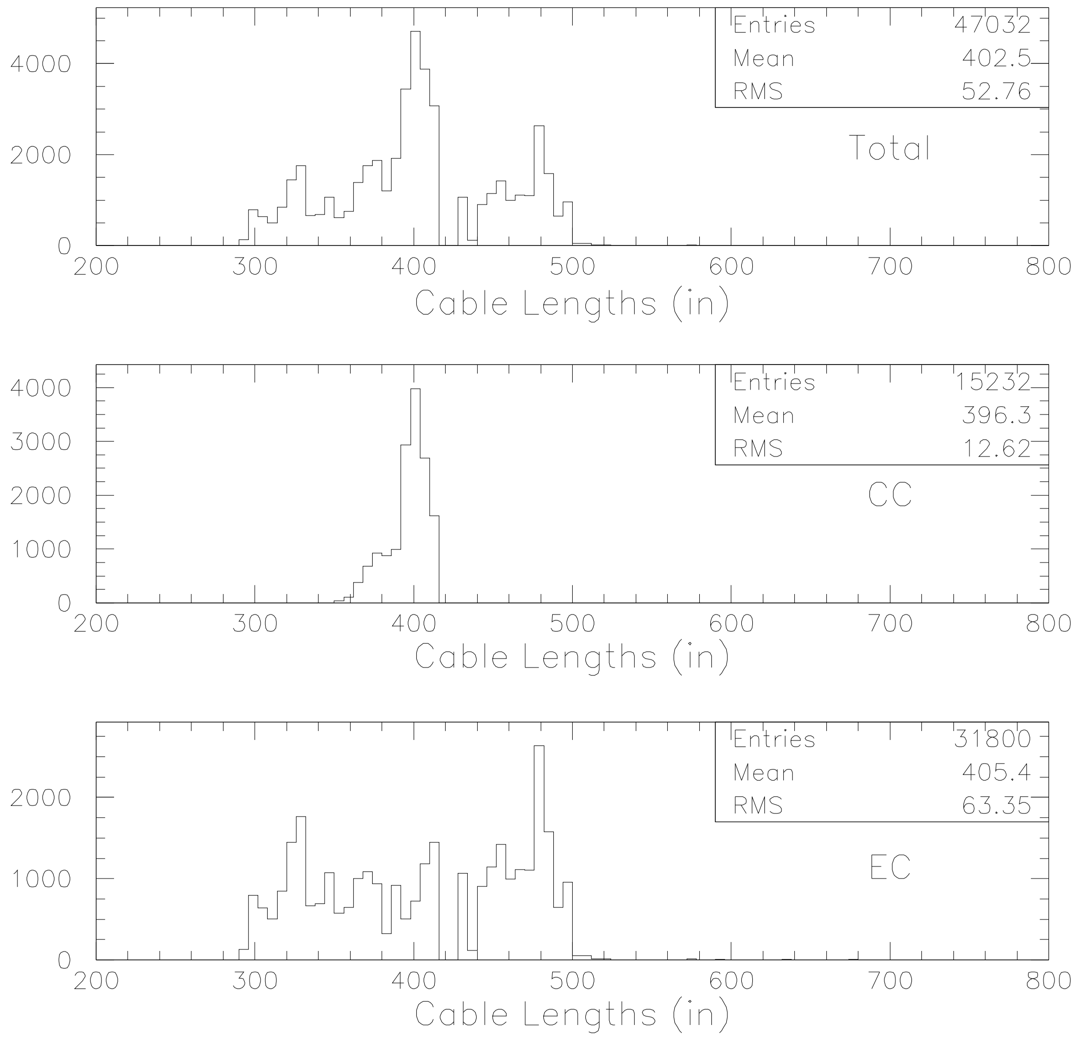

Figure 4: Distribution of preamplifier input cable length for all channels (top), CC channels only (middle) and EC channels only (bottom). This is for the Run 2 cables.

to the pedestal width is provided by the thermal noise due to the capacitance at the preamplifier input. If there is a break in the readout cable, this source of noise is not visible to the preamplifier, hence the pedestal width is reduced with respect to the width recorded using the original cables, or the new cables prior to the breakage. A second method of detecting cable breaks relies on the calibration pulses injected at the input to the preamplifiers. Some fraction of this charge remains on the detector capacitance and the readout cable, resulting in an apparently smaller preamplifier gain compared to the same preamplifier with no cable or detector capacitance connected to its input. Therefore a comparison of the measured preamplifier gains before and after replacing the external cables can also used to reveal suspected cable breaks.

The channels isolated in this way are then explicitly checked for broken cables using a device called Time Domain Reflectometer. This device is used to send electrical pulses from the preamplifier input towards the detector cells, and sense the reflection (due to change in impedance) from the other end of the readout cable. The time it takes to receive the reflection can be used to measure the length of the co-axial cable. Comparing this with the expected length indicates where a potential problem might exist.

The results of these studies are encouraging. So far only five broken contacts have been found (out of cables replaced for approximately 55,000 channels), out of which two have been fixed. Monitoring studies are performed periodically to check if the number of broken contacts increases with time. We perform calibration runs to record the pedestals, pedestal widths and gains for all channels. Using calibration data taken with the old cables, one can predict the calibration values one expects with the new cables in place. Once a calibration run with the new cables satisfies the predicted values, this run is used as a basis for comparison with future calibration runs to determine the stability of the new cables. The broken contacts will be repaired prior to the start of Run 2.

We expect the thermal noise generated by the preamplifier input cables and our sensitivity to this noise to be different in Run 2 compared to Run 1. The 30 Ω cables have higher capacitance per unit length than the 115 Ω cables, and on average are longer in Run 2, hence they generate more noise. However, since the cables exhibit the characteristics of a lumped capacitance only on time scales long compared to their propagation delay, and behave as transmission lines on short time scales, they generate thermal noise at low frequencies only. In Run 2 the shaping time is reduced, thereby accepting only higher frequencies. Hence the sensitivity to the thermal noise generated by the cables is reduced in run 2.

4.2 Preamplifier Hybrids (WBS 1.2.1.1.2)

The preamplifiers are integrating circuits that convert the image charges produced by the calorimeter cells to voltages that are proportional to the input charge. The preamplifier used in Run 1 is essentially a high gain amplifier, with the input stage designed to achieve low noise levels, high DC input impedance and very low input bias currents.

A schematic of the Run 2 preamplifier circuit is shown in figure 5. The 2SK369

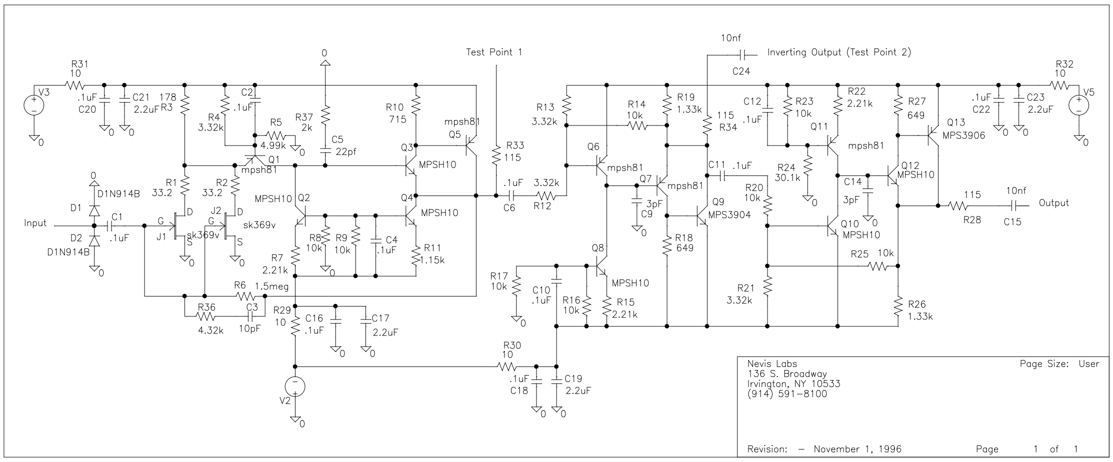

Figure 5: Schematic of the calorimeter preamplifier circuit.

junction field effect transistor (jFET) built by Toshiba was used in Run 1 and will be used again in Run 2 to form the input stage of the preamplifier. The transconductance of this jFET has been measured to be 0.046 Ω^{-1} [4]. In the Run 1 version, a single jFET was used at the input with an equivalent noise density of 0.46 nV / $\sqrt{\text{Hz}}$, resulting in single channel noise that can be characterized as 2000 + 3100 $\times$ C (nF) electrons, where C is the capacitance at the preamplifier input. In run 2, the pulse shaping time is reduced from 2.2 μs to $\sim$400 ns, resulting in a corresponding increase in electronic thermal noise (which scales as $\sqrt{\text{bandwidth}}$ and hence as $1/\sqrt{\text{shaping time}}$). To help compensate for this increased electronic noise, two jFETs in parallel will be used at the input, to reduce the noise by a factor of $1/\sqrt{2}$. The readout cable is coupled to the gate of the jFETs through a decoupling capacitor. Over-voltage and under-voltage protection at the input is provided by two back-to-back diodes connecting the input to ground.

The preamplifier for the upgrade consists of three stages, each of which is essentially a fast inverting operational amplifier. In the run 1 version, only the first stage was needed since it was not necessary to drive a fast pulse into a terminated 115 Ω cable. In the upgrade, the need to prevent reflections on the time scale of 132 ns necessitates cable termination. Since the preamplifier output is also back-terminated, a large current drive capability with twice the output voltage swing is required. To achieve these goals without compromising the first stage performance, the second and third driver stages were added. The purpose of adding two stages is two-fold. Firstly, the two inverting stages revert the polarity of the signal to the required sign. Secondly, the option is available to provide differential preamplifier output (unlike the run 1 version), by using the outputs of the second and third stages as the differential pair [2]. For this reason, the second stage is configured with a gain of -3, while the third stage is configured with a gain of -1. In order to achieve the larger voltage swing, the driver stages are powered from +12 V and -6 V, while the first stage is powered from +8 V and -6 V. All stages are internally AC-coupled through large capacitors to the following stages.

The first stage needs to accomplish a number of tasks while meeting certain requirements. It acts as a charge sensitive amplifier by using a capacitor in feedback to integrate the incoming current pulse to produce a voltage proportional to the integrated charge. The input impedance of the preamplifier must be 30 Ω to match the impedance of the input cable, to prevent the signal from reflecting. The first stage also compensates for the effect of the capacitance of the detector cell on the signal shape.

One of two values of feedback capacitors is used for the preamplifiers depending on the tower depth of the channel. EM3 and EM4 channels typically produce more charge than channels at other depths, due to their proximity to the electromagnetic shower maximum and large number of samples they sum (7 and 10 respectively). 10 pF capacitors are used in feedback for these channels. 5 pF capacitors are used for EM1, EM2 and the hadronic channels. This scheme was used in Run 1 to adjust the preamplifier gains to reduce the variation in the maximum output voltage produced by the different channels in a tower. The same scheme will be used for Run 2.

A large resistor is connected in parallel with the feedback capacitor to bleed away the stored charge, in order to prevent the preamplifier first stage output from drifting to the power rail. The resistor value is matched to the capacitor value to give a nominal decay time constant of 15 μs for all channels (unlike in Run 1 when the same resistor was used for all channels). This decay time constant in run 2 is smaller by a factor $\mathcal{O}(10)$ compared to Run 1 to account for the higher luminosity expected.

Compensation for the effects of the detector capacitance is achieved by replacing the integrating capacitor in feedback with a resistor and capacitor in series. The RC circuit has the effect of turning the first stage into an imperfect integrator, having the same effect as partially differentiating the fully integrated output. The partial differentiation compensates for the partial integration performed on the signal by the detector RC network (the detector capacitance and the cable impedance). The goal is to make the preamplifier output waveform as similar as possible for all channels, by customizing the preamplifier RC compensation to the detector capacitances of the various cells. By studying the pattern of detector capacitance, we have classified all the calorimeter cells into 14 categories [5]. We will build 14 species of preamplifiers, geared to compensate

[2]Exercising this option would require replacement of preamplifier and additional BLS backplanes, the new preamplifier motherboards, and possibly the BLS shaper. This option is kept in case of unforseen noise sources.

for the detector capacitance in the following categories of cells: electromagnetic layers 1 and 2, EM layer 3, EM layer 4 and the hadronic layers, with further categorization into central calorimeter and end-cap calorimeter cells wherever appropriate. Table 1 gives the mean and rms of the detector capacitance of the cells connected to each of these preamplifier species. The table also gives the values of those components that change from one species to another. The capacitance of EM1, EM2 and EM3 cells is about

Table 1: Detector capacitance for the various preamplifier species and the circuit component values.

Species label	Raw Cap (pF)	w/ Offset (pF)	RMS (pF)	R3 (Ω)	R36 (Ω)	R37 (Ω)	R6 ($M\Omega$)	C3 (pF)	C5 (pF)
A	416	16	150	238	0	0	3	5	10
B	1265	865	218	218	5190	2600	3	5	10
C	2182	1782	420	195	10690	5350	3	5	10
D	4028	3628	594	120	21770	6590	3	5	10
E	403	3	43	239	0	0	1.5	10	22
F	881	481	159	227	1440	660	1.5	10	22
G	1458	1058	176	213	3170	1440	1.5	10	22
Ha	1974	1574	26	200	4720	2150	1.5	10	22
Hb	2296	1896	39	193	5690	2590	1.5	10	22
Hc	2597	2197	143	185	6590	3000	1.5	10	22
Hd	2837	2437	43	179	7310	3320	1.5	10	22
He	3185	2785	77	171	8360	3800	1.5	10	22
Hf	3604	3204	48	161	9610	4370	1.5	10	22
Hg	4088	3688	85	149	11060	5030	1.5	10	22
I (ICD)	0	N/A	0	178	0	0	0.682	22	22

400 pf, EM4 about 1.5 nF, and hadronic cells about 4.5 nF. The associated RC time constants will then be about 12 ns, 45 ns, and 135 ns respectively. Compared to the 400 ns pulse shaping time, one can see that the RC delay for EM4 and the hadronic layers is not negligible. Furthermore, the shaping time for the trigger output is 132 ns, so that one would have to incorporate various sampling weights in the trigger hardware if the preamplifiers did not provide compensation, particularly for the hadronic layers.

Prototypes of preamplifiers with this compensation scheme have been built, and their frequency response was measured using a Hewlett-Packard Network Analyser. The measured frequency transfer function for various amounts of compensation is shown in figures 6 and 7. The devices exhibit the appropriate reduction of gain with frequency for an integrator, with a flattening out of the gain at high frequencies for the compensated preamplifiers. At very high frequencies the gain rolls off due to intrinsic and built-in speed limitations of the preamplifiers.

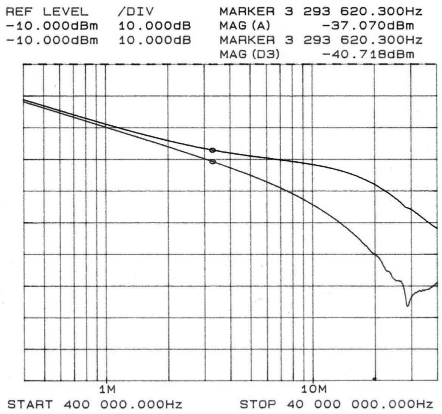

Figure 6: Log-Log plot of the measured frequency transfer functions for an uncompensated preamplifier (lower curve) and a preamplifier compensated for a detector capacitance of 667 pF (upper curve).

The process of differentiating any electronic waveform tends to make the waveform more noisy, particularly in a system with feedback such as the preamplifier stages. Preliminary tests with 120 prototypes indicate satisfactory noise performance with the circuit described above. Figure 8 shows the pedestal width in ADC counts measured for the new preamplifiers, scaled down by a factor of 3 to compensate for the gain of the driver stage, and scaled up by $\sqrt{2}$ to compensate for the presence of two jFETs. This facilitates the comparison of the noise performance with the run 1 preamplifiers (see figure 12). We find the pedestal width distribution to agree with expectations. Figure 9 shows the correlation coefficient between pedestal readings of preamplifier pairs, which is sensitive to correlated noise. The measurements show no evidence of correlated noise at this level of sensitivity.

The characteristic 30 Ω input impedance of the preamplifier is achieved by making the gain of the first stage the appropriate function of frequency. For a perfectly integrating (i.e. uncompensated) preamplifier, the feedback element through which the input current flows is a capacitor. The input can then be made to look purely resistive by using a capacitive load for the input transconductance jFETs. The product of the transconductance of the jFETs and the ratio of the internal load capacitance and the feedback capacitance sets the input impedance. For compensated preamplifiers, a resistor of the appropriate value is added in series with the load capacitor to tune the open loop gain for the feedback RC in order to maintain a purely resistive input impedance. The input impedance is measured by plotting the ratio of the frequency transfer function with and without a 30 Ω resistor connected to the preamp input. If the preamplifier input impedance were also 30 Ω, the ratio would be 0.5 or -6 dB independent of fre-